

Personalized Electronic Signature Technology Based on Stress Luminescent Materials

Zhangnan WANG *

China Cultural Relics Information Consulting Center, Beijing 100029, China

<http://doi.org/10.5755/j02.ms.39962>

Received 28 December 2024; accepted 26 December 2024

Electronic signatures play a crucial role in verifying signer identities, but their lack of personalized information increases the risk of forgery. To address this issue, a stress luminescent material based on $\text{NaNbO}_3:\text{Pr}^{3+}$ was developed and applied in anti-counterfeiting devices. Experimental results demonstrate that compared to undoped NaNbO_3 , the Pr^{3+} -doped material exhibits new absorption peaks within the 350–500 nm range. The stress luminescence intensity of the material increases initially and then decreases with rising annealing temperatures and Pr^{3+} doping concentrations. The optimal annealing temperature and doping concentration, yielding the highest stress luminescence intensity, were identified as 1075 °C and 0.7 %, respectively. Additionally, while the luminescence intensity of $\text{NaNbO}_3:\text{Pr}^{3+}$ diminishes with repeated friction, its luminescence performance is restored after UV irradiation. In anti-counterfeiting device testing, the device incorporating 1075 °C annealed $\text{NaNbO}_3:0.7\% \text{Pr}^{3+}$ was able to effectively capture variations in the writer's force during the writing process. This capability reflects the writer's unique writing habits, thereby enhancing the anti-counterfeiting effectiveness of electronic signatures. These findings indicate that the proposed $\text{NaNbO}_3:\text{Pr}^{3+}$ stress luminescent material can effectively encode personalized information in electronic signatures, significantly improving their anti-counterfeiting performance.

Keywords: electronic seal, electronic signature, anti-counterfeiting, stress luminescent materials, $\text{NaNbO}_3:\text{Pr}^{3+}$.

1. INTRODUCTION

As Internet technology continues to advance, network activities are becoming increasingly frequent, and electronic signatures are now widely adopted across various fields as a standard anti-counterfeiting measure. An electronic signature comprises data in electronic form, attached to a data message to identify the signatory and indicate their consent to the message's content. Unlike a simple digital representation of a handwritten signature, electronic signatures typically record only the static characteristics of signatures during their creation. This limitation makes electronic signatures vulnerable to increasingly sophisticated forgery techniques.

Stress-luminescent materials, which emit light when subjected to mechanical stimulation, offer a promising solution to enhance the personalization and security of electronic signatures [1, 2]. The intensity of their luminescence corresponds to the degree of mechanical stimulation, enabling them to capture dynamic information during the signing process. However, traditional high-temperature solid-phase synthesis methods for preparing stress-luminescent materials often result in poor control over the size and morphology of the materials, limiting their practical applications. Additionally, the large specific surface area of nanomaterials introduces defects that weaken the performance of stress-luminescent materials [3–4].

To address these challenges and elevate the anti-counterfeiting capabilities of electronic signatures, this study proposes the preparation of stress-luminescent materials based on $\text{NaNbO}_3:\text{Pr}^{3+}$ using a hydrothermal-

annealing method. This approach aims to enhance the performance of stress-luminescent materials, promote their practical application, and advance research in the field of anti-counterfeiting.

The study comprises three main parts: the first focuses on the preparation and testing methods of $\text{NaNbO}_3:\text{Pr}^{3+}$; the second analyzes the performance test results of the material; and the third provides a comprehensive summary of the findings.

2. MATERIALS AND METHODS

2.1. Experimental materials and equipment

The materials used in this study included niobium oxide, praseodymium oxide, absolute ethanol, sodium hydroxide, deionized water, silicone, and activated carbon. Detailed specifications of these materials are presented in Table 1.

Table 1. Purity and manufacturer of the materials

Name	Purity	Manufacturer
Columbium oxide	99.99%	Aladdin Reagents Ltd
Praseodymium	99.99%	Aladdin Reagents Ltd
Absolute ethyl alcohol	Analytical reagent	Tianjin Tianli Reagent Co., Ltd
Caustic soda	99.99%	Aladdin Reagents Ltd
Deionized water	–	Aladdin Reagents Ltd
Silicone	–	Tianjin XinSpecial Chemical Co., LTD
Acticarbon	Analytical reagent	Dow Corning Corporation, USA

* Corresponding author: Z.Wang
E-mail: WangZhangnan@CCRICC.org.cn

Niobium oxide, praseodymium oxide, and sodium hydroxide were of 99.99 % purity, while absolute ethanol and activated carbon met analytical grade purity requirements. The models of the experimental equipment are detailed in Table 2.

Table 2. Model type and manufacturer of the experimental equipment

Device name	Version	Manufacturer
X-ray diffractometer	X'PERT	Panalytical Analytical Instruments, the Netherlands
X-ray photoelectron spectrometer	5700 ESCA	AutoInte (PHI)
UV-visible near-infrared spectrophotometer	Cary-5000	Agilent
Steady-state / transient fluorescence spectrometer	FLS-1000	Edinburgh
Field emission scanning electron microscope	Supra55	Carl Zeiss
Optical fiber spectrometer	SR500i-A	UK Andor Inc
Electronic balance	321LS	Swiss Precisa Inc
Bunsen beaker	50 ml	Sichuan Shubo (Group) Co., LTD
Corundum crucible	30 ml	Shanghai Pengcheng Special Ceramics Co., LTD
Muffle furnace	CHY-1500	Henan Chengyi Laboratory Equipment Co., LTD
Magnetic stirring apparatus	IKA C-MAG HS7	IKA Instruments, Germany
Centrifuge	H1850	Xiangyi Centrifuge Instrument Co., Ltd
Electrothermal blowing dry box	DHG-9075A	Shanghai Yiheng Scientific Instrument Co., LTD
Plastic packaging machine	Deli-3895	Deli Group Company Limited

2.2. Experimental methods

2.2.1. Preparation of luminescent materials

The luminescent material, $\text{NaNbO}_3:\text{Pr}^{3+}$, was synthesized using a two-step process involving hydrothermal synthesis and high-temperature annealing. The precursor material was first prepared via a hydrothermal method, followed by annealing to produce the desired luminescent material. The doping concentration of Pr^{3+} (denoted as x) was varied as 0.1 %, 0.3 %, 0.5 %, 0.7 %, and 1 %. Materials annealed at different temperatures were designated as $\gamma\text{-NaNbO}_3:\text{Pr}^{3+}$, while materials with varying doping concentrations were referred to as $\text{NaNbO}_3: x\text{Pr}^{3+}$.

The preparation procedure involves accurately weighing 1.6613 g of niobium oxide, 8.4 g of sodium hydroxide, and the required amount of praseodymium oxide using an electronic balance. These materials are then added to 25 mL of deionized water in a beaker and stirred for 3 hours using a magnetic stirrer to ensure thorough mixing. The resulting mixture is transferred into a PTFE-lined reactor and subjected to a hydrothermal reaction at 200 °C for 6 hours [5–7]. After the reaction, the products are washed with deionized water until the pH becomes neutral, followed by drying at 60 °C for 24 hours [8–10]. The dried

precursor is placed into a corundum crucible and annealed at different temperatures for 4 hours in a muffle furnace. Finally, the material is allowed to cool to room temperature within the furnace to yield the luminescent material.

2.2.1 Preparation of anti-counterfeiting devices

The anti-counterfeiting device was fabricated by mixing $\text{NaNbO}_3:\text{Pr}^{3+}$ with polydimethylsiloxane (PDMS) at a weight ratio of 1:3. The mixture is then transferred to an oven and maintained at 80 °C for 2 hours. After cooling to room temperature, the anti-counterfeiting pattern can be peeled off. For more complex patterns, multiple casting processes may be required to achieve the desired result.

2.3. Material characterization methods

The crystal structure of the synthesized materials was determined using an XRD at room temperature. Cu-K_α radiation with an emission power of 2.2 kW was used as the source. The scanning speed was set to 3°/min, and the scan range was 20–80°. The diffraction patterns were analyzed using Jade 6 software to identify the crystal structure.

The surface morphology of the materials was observed using a field emission scanning electron microscope (FESEM) [11–13].

The atomic valence states of the materials were analyzed using an XPS with an Al-K_α radiation source. The scanning range was 0–1350 eV.

The optical absorbance characteristics were measured using a UV-Vis-NIR spectrophotometer over the range of 200–800 nm. The light source was a combination of a deuterium lamp (180–350 nm) and a tungsten lamp (350–3300 nm), with a light source switching position at 350 nm. A photomultiplier tube was used as the detector.

The luminescence properties were evaluated using a fluorescence spectrometer. The emission and excitation spectra ranged from 550–750 nm and 250–500 nm, respectively. Fluorescence lifetimes were measured at 611 nm using a xenon lamp and microsecond lamp sources [14–16].

The stress emission spectrum was recorded using a fiber optic spectrometer. Before testing, the materials were irradiated with a 365 nm UV lamp (6 W) for 1 minute. Testing commenced 1 minute after irradiation.

Material defects were analyzed using a thermoluminescence meter. The sample was heated from 40 °C to 250 °C at a rate of 2 °C/s. Before testing, the material was irradiated with a 365 nm UV lamp (6 W) for 1 minute.

3. RESULTS AND DISCUSSION

3.1. Analysis of stress-luminescence properties of materials

The XRD diffraction patterns of $\text{NaNbO}_3:\text{Pr}^{3+}$ at varying annealing temperatures and Pr^{3+} doping levels are presented in Fig. 1. In Fig. 1 a, the diffraction peaks of the prepared $\text{NaNbO}_3:0.5\% \text{Pr}^{3+}$ stress-luminescent material align closely with the standard pattern, indicating high purity with no detectable impurities. The material was confirmed as a pure orthorhombic phase of NaNbO_3 . After annealing, preferential growth was observed in the (141)

crystal plane of $\text{NaNbO}_3:0.5\% \text{Pr}^{3+}$, suggesting that Pr^{3+} ions replaced Na^+ ions in the crystal lattice due to their similar ionic radii. In Figure 1b, the diffraction peak near 32° gradually shifted towards higher angles with increasing Pr^{3+} doping levels. This rightward shift indicates lattice contraction caused by the substitution of Na^+ ions with Pr^{3+} ions, further confirming successful doping.

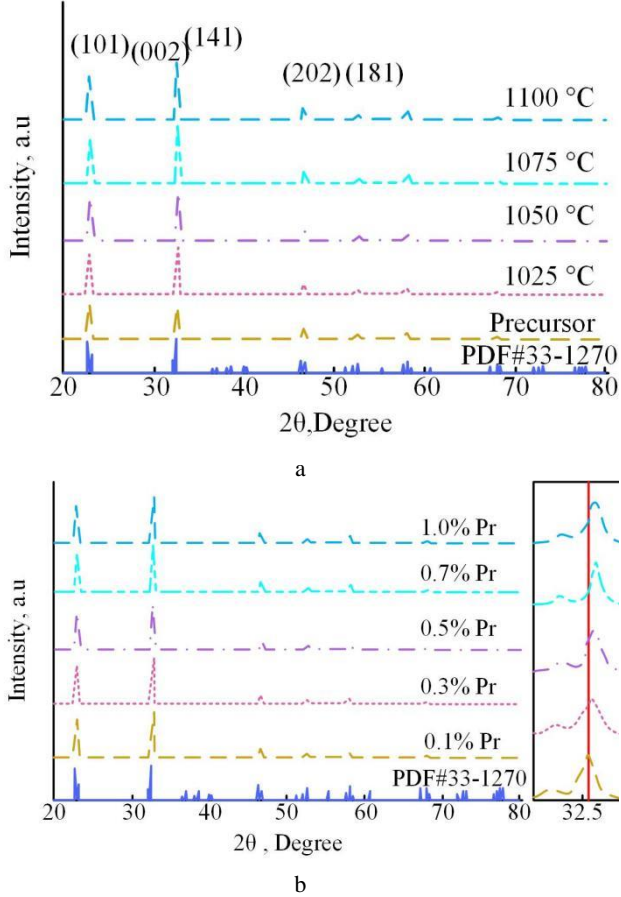


Fig. 1. XRD diffraction patterns of $\text{NaNbO}_3:\text{Pr}^{3+}$: a–XRD patterns at different annealing temperatures; b–XRD patterns at varying Pr^{3+} doping levels

SEM images of $\text{NaNbO}_3:\text{Pr}^{3+}$ synthesized under different conditions are shown in Fig. 2. In Fig. 2 a, the precursor of $\text{NaNbO}_3:0.5\% \text{Pr}^{3+}$ exhibited a cubic morphology. With increasing annealing temperatures from 1025°C to 1075°C , the surface smoothness improved without significant changes in size. At 1100°C , crystal growth resumed, with observable crystal steps and a size increase to approximately $1\ \mu\text{m}$. In Fig. 2 b, the doping levels of Pr^{3+} had a minimal impact on the crystal shape and size, indicating that the crystal morphology of $\text{NaNbO}_3:\text{Pr}^{3+}$ remains largely unaffected by doping concentration.

The UV-visible diffuse reflectance spectra of $\text{NaNbO}_3:\text{Pr}^{3+}$ materials under varying annealing temperatures and Pr^{3+} doping levels are shown in Fig. 3. In Fig. 3 a, a new absorption peak in the range of $350\text{--}500\ \text{nm}$ was observed for Pr^{3+} -doped materials, attributed to the electronic transition of Pr^{3+} ions from the ground to excited states. As the annealing temperature increases, a redshift of the absorption edge is observed for $\text{NaNbO}_3:0.5\%\text{Pr}^{3+}$, which can be attributed to crystal growth and the resulting increase in crystal size caused by higher annealing temperatures.

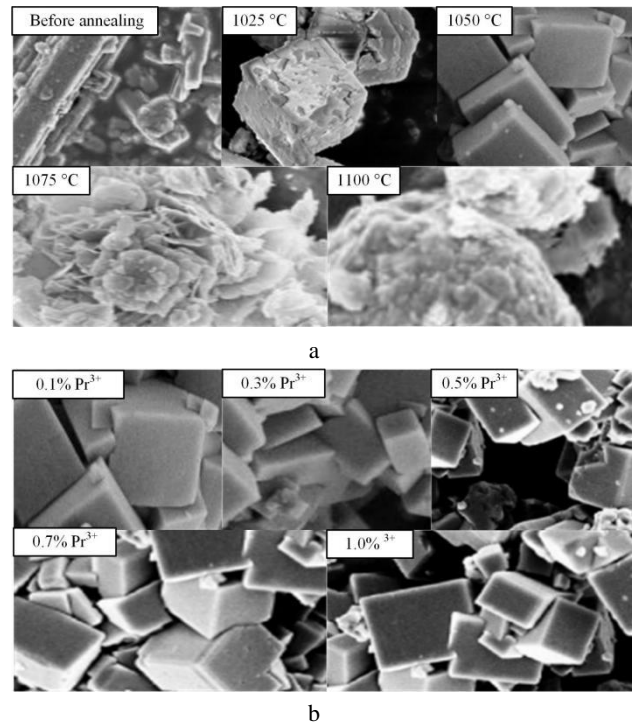
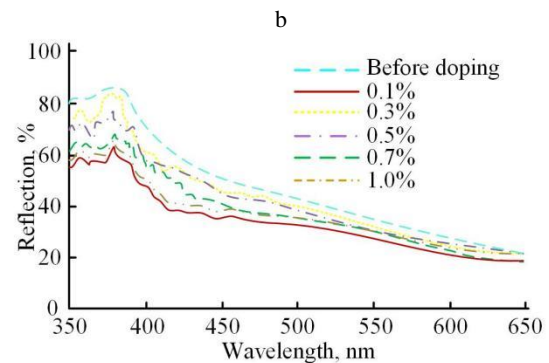
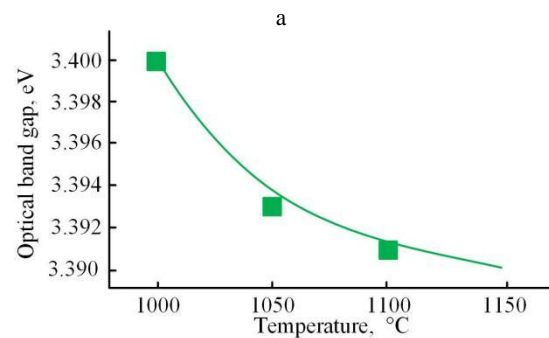
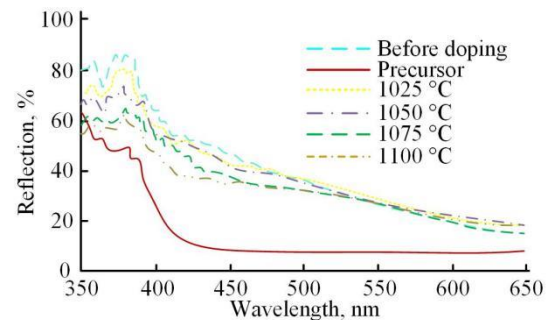


Fig. 2. SEM images of $\text{NaNbO}_3:\text{Pr}^{3+}$: a–SEM images at different annealing temperatures; b–SEM images at varying Pr^{3+} doping levels



continued on the next page

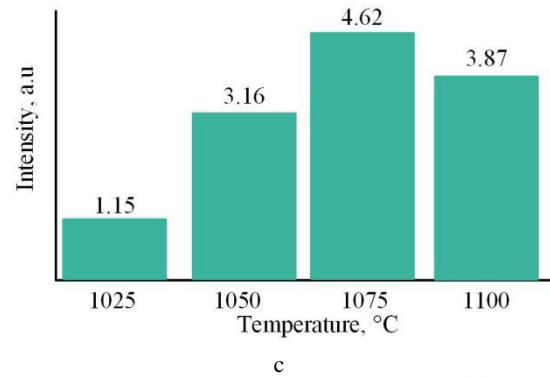
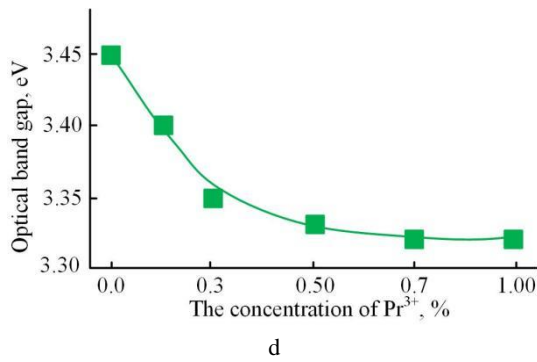


Fig. 3. UV-visible diffuse reflectance spectra of $\text{NaNbO}_3:\text{Pr}^{3+}$: a–diffuse reflectance spectra at varying annealing temperatures; b–optical bandgap changes with annealing temperature; c–diffuse reflectance spectra at varying Pr^{3+} doping levels; d–optical bandgap changes with Pr^{3+} doping levels

In Fig. 3 b, the optical bandgap of $\text{NaNbO}_3:\text{Pr}^{3+}$ decreased from 3.4 eV to 3.39 eV with rising annealing temperatures, consistent with crystal size enlargement. Similarly, in Fig. 3 c, the absorption edge red-shifted and absorption intensity increased with higher Pr^{3+} doping levels. The optical bandgap also decreased from 3.45 eV to 3.34 eV (Fig. 3 d), which is attributed to the size enhancement induced by doping.

The luminescence performance test results of $\text{NaNbO}_3:\text{Pr}^{3+}$ synthesized under different annealing temperatures and Pr^{3+} doping levels are illustrated in Fig. 4. In Fig. 4 a, a strong excitation band appears in the range of 300–350 nm, attributed to the lattice absorption of NaNbO_3 . The excitation band within 350–375 nm is associated with charge transfer, while the weaker excitation band between 375–425 nm is linked to the absorption of Pr^{3+} ions and transitions involving the $^3\text{P}_2$, $^3\text{P}_1$, and $^3\text{P}_0$ energy levels.

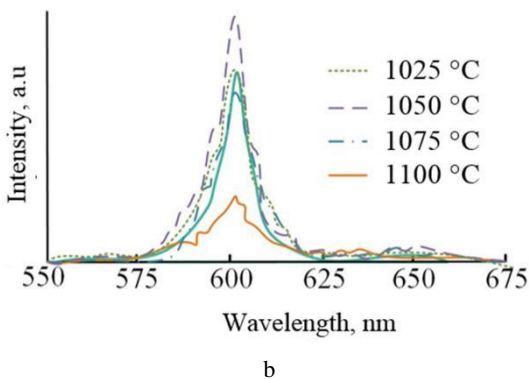
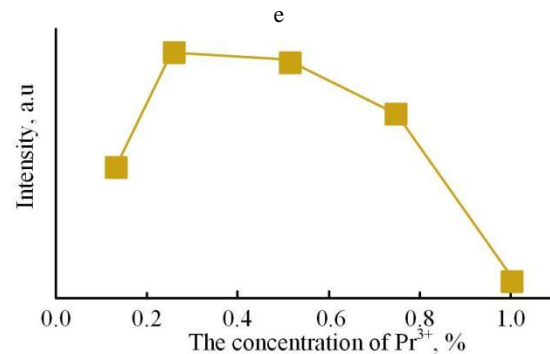
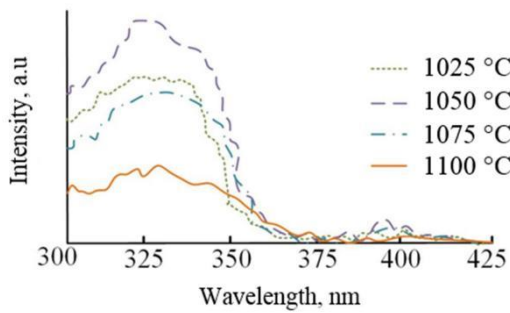
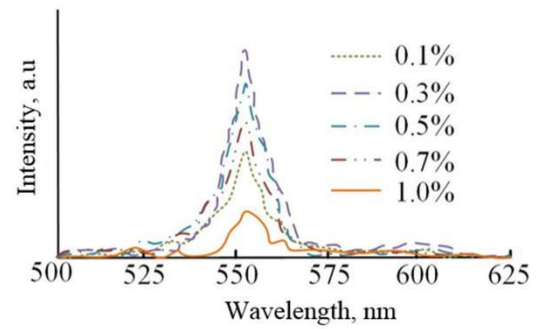
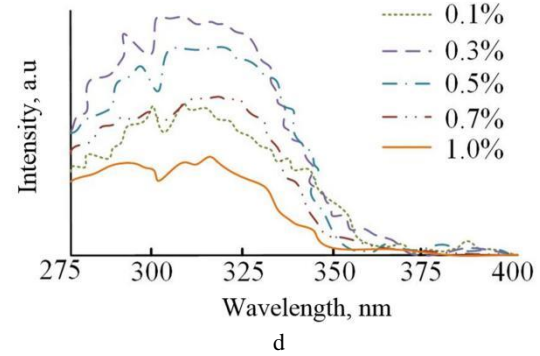


Fig. 4. Luminescence performance test results of $\text{NaNbO}_3:\text{Pr}^{3+}$: a, b, c–represent excitation spectra, emission spectra, and emission intensities at different annealing temperatures, respectively; d, e, f–depict excitation spectra, emission spectra, and emission intensities at varying Pr^{3+} doping levels

As shown in Fig. 4 b, the emission peaks for $\text{NaNbO}_3:0.5\%\text{Pr}^{3+}$ across different annealing temperatures consistently occur at 607 nm, arising from the electronic transitions of Pr^{3+} ions. In Fig. 4 c, it is evident that the emission intensity of $\text{NaNbO}_3:0.5\%\text{Pr}^{3+}$ initially increases and then decreases with rising annealing temperatures, peaking at 1075 °C. Fig. 4 d shows that the excitation

intensity of $\text{NaNbO}_3:\text{Pr}^{3+}$ first increases and then decreases as the Pr^{3+} doping concentration rises, reaching a maximum at a doping level of 0.3 %. Similarly, Fig. 4 e and f reveal a trend where the emission intensity increases and then decreases as Pr^{3+} doping levels rise, with the optimal Pr^{3+} concentration for maximum emission being 0.3 %.

The stress-luminescence behavior of $\text{NaNbO}_3:\text{Pr}^{3+}$ under varying annealing temperatures is presented in Fig. 5.

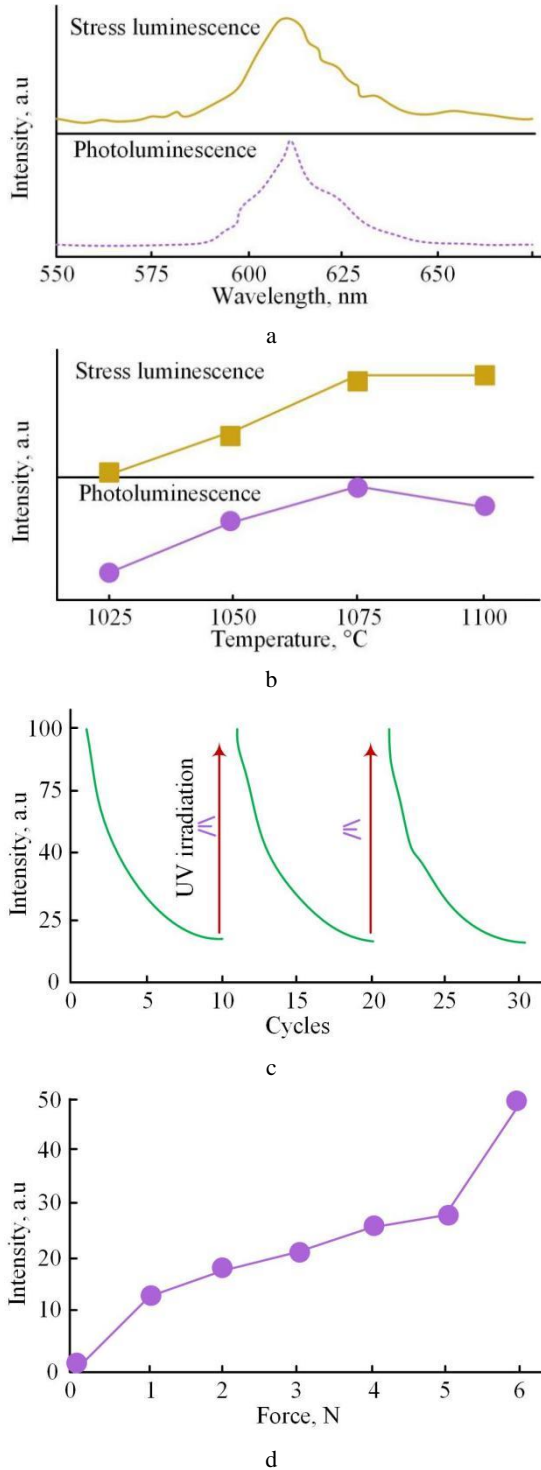
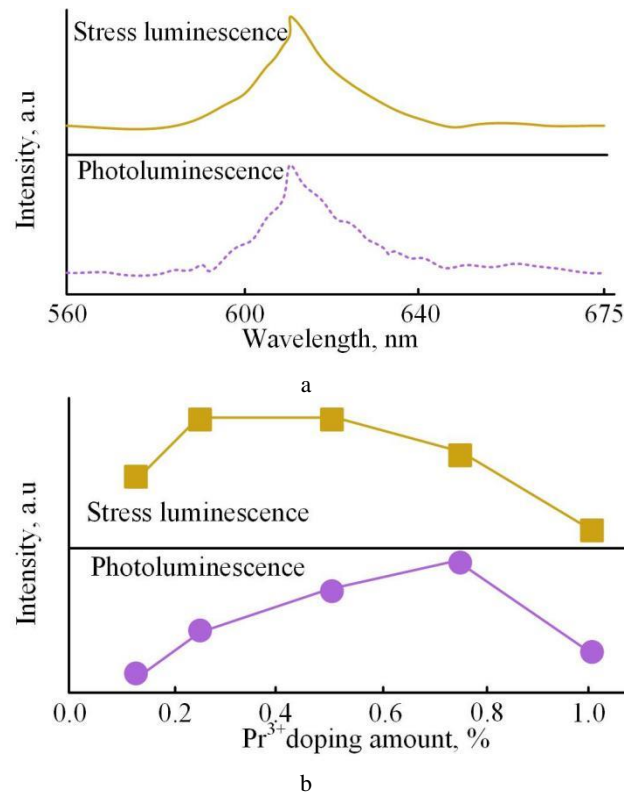


Fig. 5. Stress-luminescence properties of $\text{NaNbO}_3:\text{Pr}^{3+}$: a, b, c, d – depict the luminescence spectrum at different annealing temperatures, the luminescence intensity-temperature relationship, irradiation recovery characteristics, and the linear relationship between luminescence intensity and applied pressure, respectively

Fig. 5 a demonstrates that the stress-induced luminescence color aligns with the photoluminescence spectrum, confirming that both phenomena originate from the electronic transitions of Pr^{3+} ions. As shown in Fig. 5 b, the stress luminescence intensity initially increases and then decreases with higher annealing temperatures, peaking at 1075°C . This pattern is consistent with the photoluminescence results. In Fig. 5 c, the luminescence intensity decreases progressively with increasing friction cycles, dropping from 100 a.u. to 14 a.u.; however, the intensity fully recovers after irradiation. This behavior indicates that the stress luminescence of $\text{NaNbO}_3:0.5\%\text{Pr}^{3+}$ is closely tied to its trap characteristics. Fig. 5 d shows a linear relationship between stress and luminescence intensity. As applied stress increases, the luminescence intensity of $\text{NaNbO}_3:0.5\%\text{Pr}^{3+}$ steadily rises, reaching 48 a.u. under stress of 6 N. These results highlight that the stress-luminescent material developed in this study exhibits not only high luminescence intensity but also excellent reproducibility, making it a promising candidate for practical applications.

The stress luminescence performance of $\text{NaNbO}_3:\text{Pr}^{3+}$ at varying Pr^{3+} doping levels is illustrated in Fig. 6. As shown in Fig. 6 a, the photoluminescence and stress-induced luminescence originate from the same mechanism – electronic transitions of Pr^{3+} ions. Fig. 6 b demonstrates that the stress-induced luminescence intensity initially increases and then decreases as the Pr^{3+} doping level rises. The maximum luminescence intensity is observed at a doping level of 0.7 %, differing from the trend observed in photoluminescence. In Fig. 6 c, the luminescence intensity diminishes progressively with increased friction cycles, declining from 100 a.u. to 14 a.u. Remarkably, UV irradiation restores the luminescence intensity to its original state.



continued on the next page

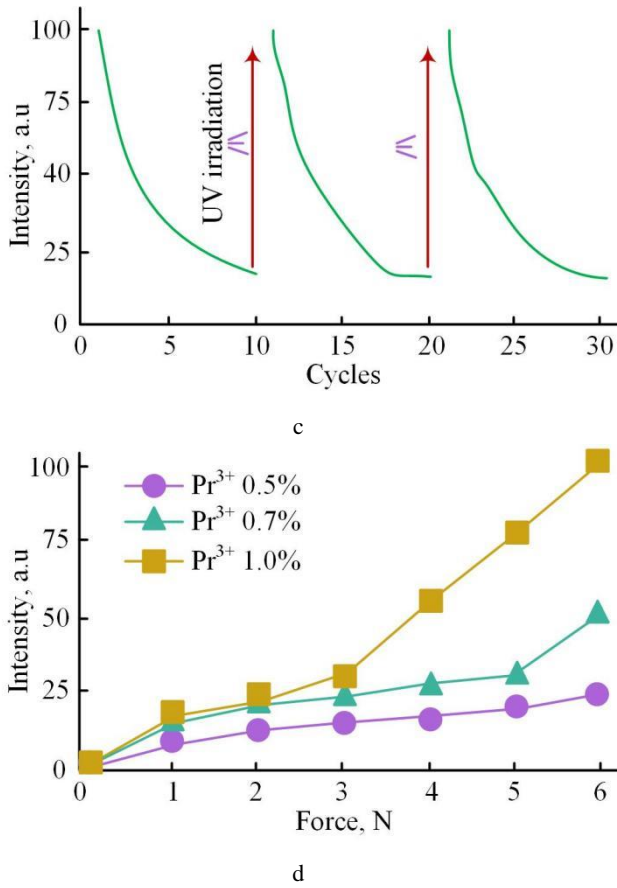


Fig. 6. Stress luminescence performance of $\text{NaNbO}_3:\text{Pr}^{3+}$: a–luminescence spectra; b–luminescence intensity vs. Pr^{3+} doping level; c–irradiation recovery; d–luminescence intensity vs. applied stress

This phenomenon occurs because UV irradiation refills the trap states with electrons, enabling them to be released again under mechanical stimulation. In Fig. 6 d, the stress luminescence intensity of all Pr^{3+} -doped materials increases with applied stress. Among these, the material with a Pr^{3+} doping concentration of 0.7 % exhibits the most significant response to increasing stress. These results demonstrate that $\text{NaNbO}_3:\text{Pr}^{3+}$ achieves optimal stress luminescence performance at a Pr^{3+} doping concentration of 0.7 %.

The thermoluminescence (TL) spectra of $\text{NaNbO}_3:\text{Pr}^{3+}$ under different annealing temperatures and Pr^{3+} doping concentrations are presented in Fig. 7. In Fig. 7 a, for $\text{NaNbO}_3:0.5\%\text{Pr}^{3+}$ synthesized at the same annealing temperature, the TL intensity initially increases and then decreases with rising operational temperatures, reaching a peak between 60 °C and 80 °C. At a fixed operational temperature, the TL intensity also follows a similar trend with an increasing annealing temperature, peaking at 1075 °C. For the sample annealed at 1075 °C, the maximum TL intensity is observed at 68 °C. Fig. 7 b illustrates that at a fixed Pr^{3+} doping concentration, the TL intensity of the material also increases initially and then decreases as the operational temperature rises. Similarly, at a fixed operational temperature, the TL intensity exhibits a peak as the Pr^{3+} doping concentration increases, reaching its maximum at 0.7% Pr^{3+} . At this doping level, the TL intensity peak occurs at 80 °C. These results indicate that both annealing temperature and Pr^{3+} doping concentration

significantly influence the thermoluminescence properties of $\text{NaNbO}_3:\text{Pr}^{3+}$. Optimal TL performance is achieved at an annealing temperature of 1075 °C and a Pr^{3+} doping concentration of 0.7 %.

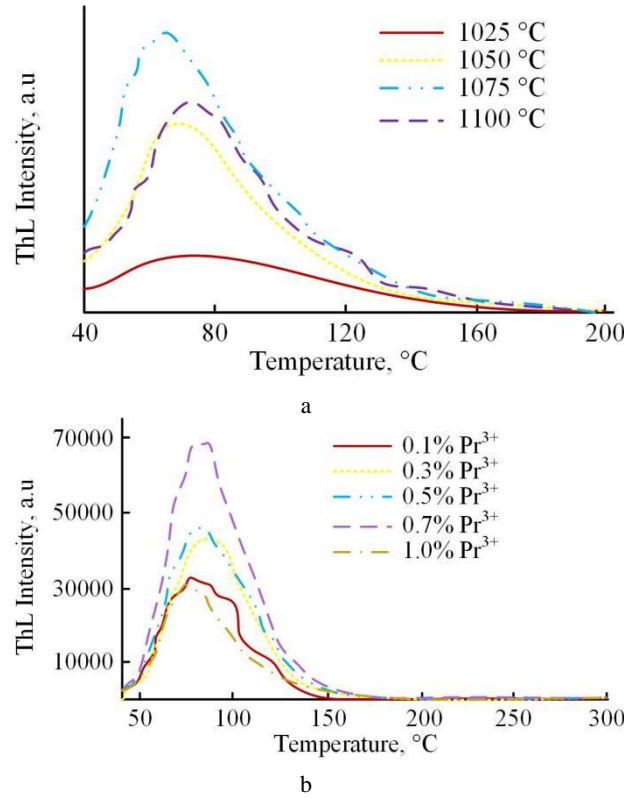


Fig. 7. Thermoluminescence spectra of $\text{NaNbO}_3:\text{Pr}^{3+}$: a–thermoluminescence spectra at different annealing temperatures; b–thermoluminescence spectra at varying Pr^{3+} doping levels

The thermal release spectral peaks and activation energies of $\text{NaNbO}_3:\text{Pr}^{3+}$ at different annealing temperatures and Pr^{3+} doping levels are summarized in Table 3.

Table 3. Thermal release spectral peaks and activation energies of $\text{NaNbO}_3:\text{Pr}^{3+}$ under varying annealing temperatures and Pr^{3+} doping levels

Annealing temperature 0.5 % Pr^{3+}	Peak temperature, K		Activation energy, eV	
	Trap 1	Trap 2	Trap 1	Trap 2
1025 °C	344.7	363.5	0.79	0.75
1050 °C	343.8	359.1	0.76	0.79
1075 °C	340.2	351.8	0.74	0.77
1100 °C	350.3	360.1	0.77	0.79
The Pr^{3+} doping amount				
0.1 %	345.8	363.5	0.76	0.75
0.3 %	352.3	375.6	0.74	0.79
0.5 %	351.5	367.6	0.78	0.82
0.7 %	354.7	369.8	0.76	0.80
1 %	351.4	376.7	0.78	0.83

The results reveal that as the annealing temperature increases, the peak temperatures of traps 1 and 2 initially rise and then decline. Correspondingly, the activation energy first decreases and then increases. At an annealing temperature of 1075 °C, the activation energies of traps 1 and 2 reach 0.74 eV and 0.77 eV, respectively. These deep traps inhibit the release of captured electrons, contributing

to enhanced stress luminescence. This finding establishes 1075 °C as the optimal annealing temperature for $\text{NaNbO}_3:\text{Pr}^{3+}$ materials. While the Pr^{3+} doping level influences the peaks and activation energies of the pyroelectric spectrum, the changes are irregular. However, the activation energy of Pr^{3+} -doped $\text{NaNbO}_3:\text{Pr}^{3+}$ materials consistently exceeds 0.75 eV, indicating that Pr^{3+} ions enhance the stress luminescence properties of NaNbO_3 .

The fluorescence lifetime of $\text{NaNbO}_3:\text{Pr}^{3+}$ at varying Pr^{3+} doping levels is illustrated in Fig. 8. As shown in Fig. 8 a, the decay intensity increases with higher Pr^{3+} doping levels, and the decay curves follow a three-exponential fitting model. Fig. 8 b reveals a trend of decreasing average fluorescence lifetime with increased Pr^{3+} doping. For example, at a doping level of 0.1 %, the average fluorescence lifetime is 1.93 ms, whereas it decreases to 1.26 ms at 0.7 % doping. This reduction is attributed to closer ion spacing with higher Pr^{3+} doping, leading to enhanced non-radiative transitions and ion interactions, which ultimately shorten the fluorescence lifetime.

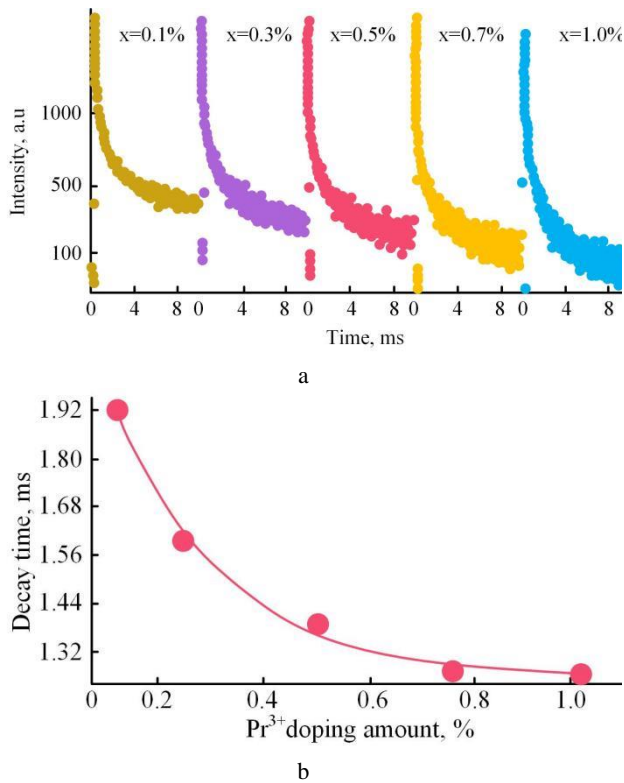


Fig. 8. Fluorescence lifetime of $\text{NaNbO}_3:\text{Pr}^{3+}$: a – decay intensity curves; b – average fluorescence lifetime for various Pr^{3+} doping levels

Taking $\text{NaNbO}_3:0.7\% \text{Pr}^{3+}$ as an example, its long afterglow properties are shown in Fig. 9. In Fig. 9 a, the long afterglow luminescence intensity initially decreases rapidly, and then stabilizes over time. By fitting the decay data, three decay time parameters – 0.24 s, 34.24 s, and 125.90 s – are obtained, indicating the presence of both shallow and deep traps. Fig. 9 b shows a gradual reduction in long afterglow luminescence intensity over time, with the decay rate significantly slowing after 30 seconds. These characteristics underscore the material's potential for applications requiring prolonged luminescence.

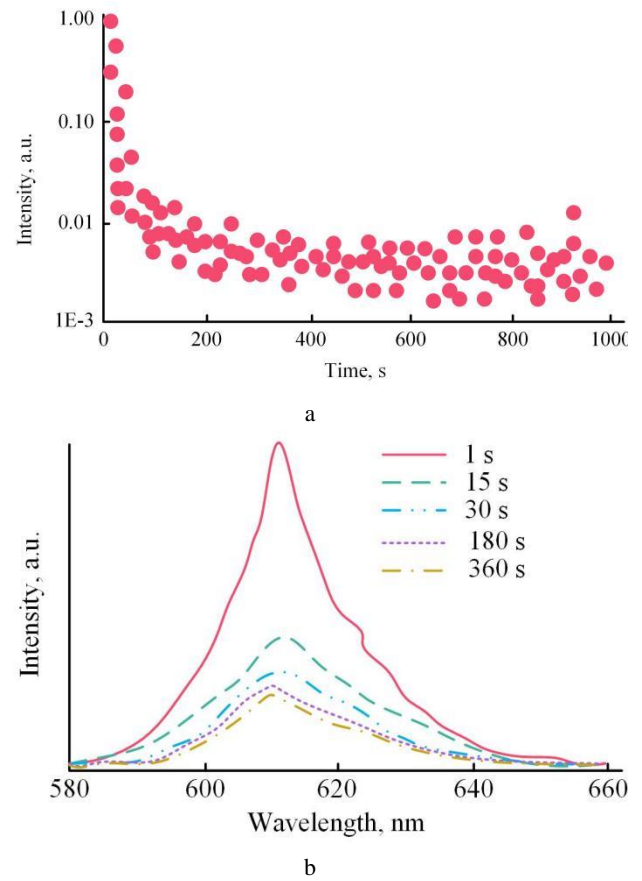


Fig. 9. Long afterglow properties of $\text{NaNbO}_3:0.7\% \text{Pr}^{3+}$: a – decay curve; b – luminescence spectrum over time

3.2. Analysis of anti-counterfeiting performance of stress-emitting devices

A novel anti-counterfeiting device based on $\text{NaNbO}_3:\text{Pr}^{3+}$ stress luminescent material is proposed. This device captures personalized dynamic information during handwriting, significantly enhancing anti-counterfeiting capabilities. Using a stress luminescence acquisition system, the performance of the anti-counterfeiting device incorporating 1075 °C annealed $\text{NaNbO}_3:0.7\% \text{Pr}^{3+}$ was evaluated. The pressure distribution results are presented in Fig. 10. In Fig. 10 a, the device emits red light under pressure, vividly reflecting the writer's handwriting. By grayscale processing the image, the two-dimensional distribution of stress luminescence intensity is obtained. Fig. 10 b highlights differences in luminescence intensity at two selected locations (Location 1 and Location 2), attributed to variations in applied pressure. These results demonstrate that the anti-counterfeiting device based on 1075 °C annealed $\text{NaNbO}_3:0.7\% \text{Pr}^{3+}$ effectively captures the force variations exerted during writing, providing insights into the writer's habits. Additionally, it records writing speed, making signature forgery significantly more challenging.

The comparison of writing effects among different writers is illustrated in Fig. 11. As shown, the anti-counterfeiting device accurately captures and reflects the writers' unique writing habits and force application patterns during the writing process.

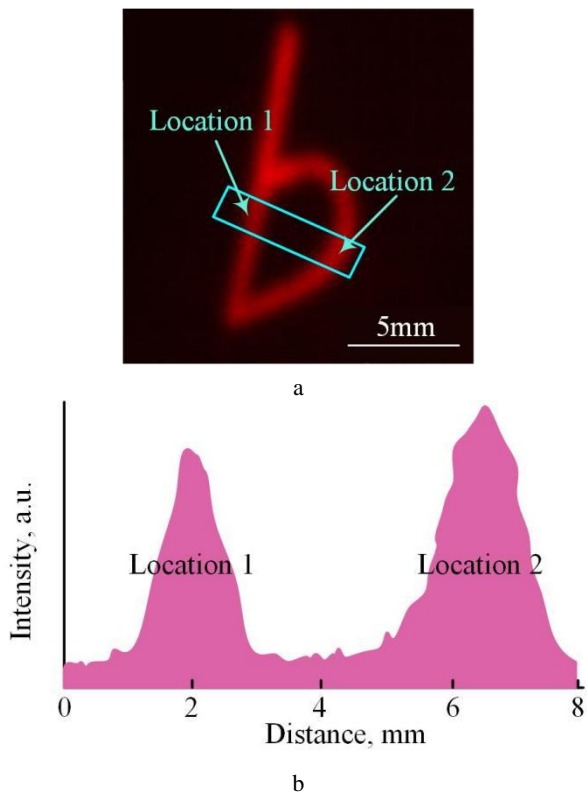


Fig. 10. Pressure distribution of the anti-counterfeiting device using 1075 °C annealed $\text{NaNbO}_3:0.7\% \text{Pr}^{3+}$: a – luminescence intensity map of handwritten text; b – selected pressure intensity distribution

For instance, Writer A demonstrates consistent force application, resulting in tidy and uniform handwriting. In contrast, Writer B exhibits uneven force application, leading to variations in handwriting depth and stroke intensity. The anti-counterfeiting device, utilizing 1075 °C annealed $\text{NaNbO}_3:0.7\% \text{Pr}^{3+}$, successfully highlights these individual writing traits. This capability offers a novel approach to electronic signature anti-counterfeiting by integrating personalized dynamic data.

3.3. Discussion

This study introduces a novel anti-counterfeiting device based on $\text{NaNbO}_3:\text{Pr}^{3+}$ stress luminescent materials for electronic signatures. To meet the requirements of electronic signatures, $\text{NaNbO}_3:\text{Pr}^{3+}$ with an annealing temperature of 1075 °C and a Pr^{3+} doping concentration of 0.7 % was selected. Experimental results demonstrate that this material exhibits a high stress luminescence intensity, exceeding 100 a.u., enabling precise recording of dynamic signing parameters such as writing speed and pressure patterns. The enhanced stress luminescence performance is attributed to Pr^{3+} doping, which improves the material's ferroelectric and piezoelectric properties, voltage constant, and transduction coefficient [18, 19]. These findings align with prior studies by Xu et al. [17], validating the effectiveness of this approach in bolstering the anti-counterfeiting capabilities of electronic signatures. Yawalkar et al. [5] investigated the mechanical luminescence of $\text{Li}_6\text{Y}(\text{BO}_3)_3: \text{Dy}^{3+}/\text{Eu}^{3+}$ phosphors. The author demonstrates that emission intensity and color can be adjusted by changing the dopant concentration, indicating

that doping plays a crucial role in optimizing stress-induced luminescence performance.

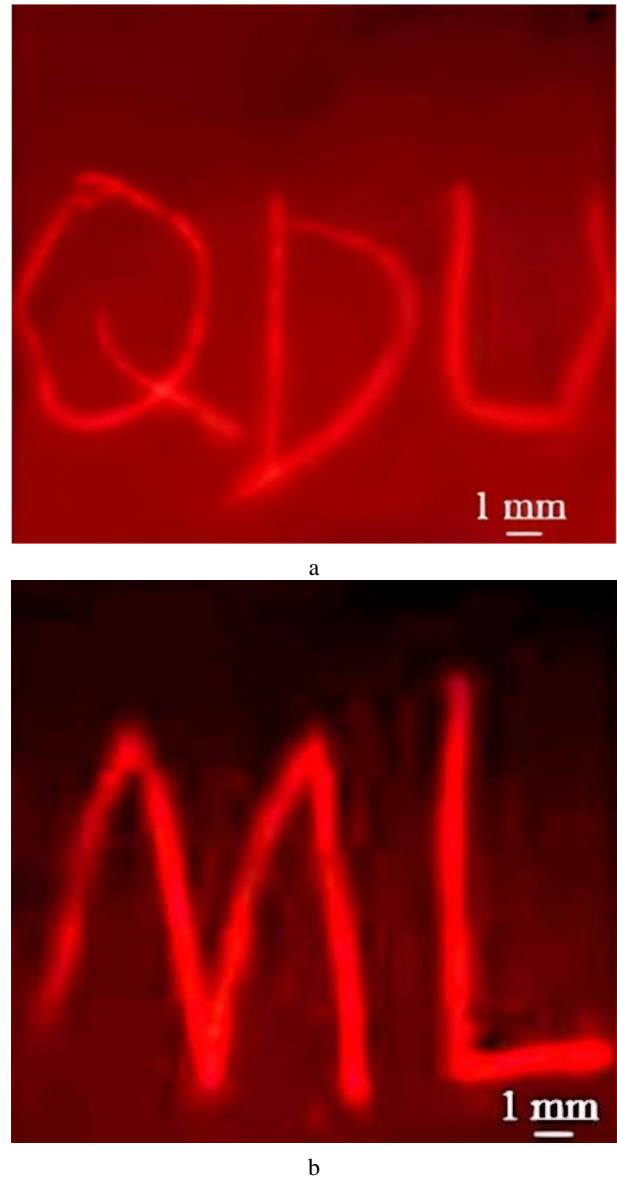


Fig. 11. Comparison of writing effects among different writers: a – Writer A; b – Writer B

This discovery is consistent with the observation of research results, that is, Pr^{3+} doping significantly improves the stress luminescence intensity and stability of NaNbO_3 .

Traditional stress luminescent materials are often constrained by limited luminescent properties and preparation challenges, which restrict their practical application in electronic signatures. In contrast, the $\text{NaNbO}_3:0.7\% \text{Pr}^{3+}$ material prepared through a hydrothermal annealing method demonstrates not only improved luminescence intensity but also controllable size, making it a promising candidate for real-world implementation. However, a notable limitation is the reduction in luminescence intensity under repeated mechanical stimuli. While this can be restored through UV irradiation, reliance on external restoration methods restricts the material's long-term applicability.

Future research should prioritize the development of stress luminescent materials with stable and enduring

performance under prolonged use, eliminating the need for external interventions. This advancement would further broaden the practical scope of such materials in anti-counterfeiting applications.

4. CONCLUSIONS

Current electronic signature systems often rely on static visual representations, such as images of handwritten signatures or stamps, which are susceptible to forgery due to their inability to capture dynamic signature traits. To address this limitation, $\text{NaNbO}_3:\text{Pr}^{3+}$ stress luminescent materials were introduced as the foundation for a novel anti-counterfeiting device. Key findings from this study include:

1. Optical and luminescent properties: Pr^{3+} doping introduces a new absorption peak in the 350–500 nm range due to electronic transitions. Both the annealing temperature and Pr^{3+} doping concentration significantly affect the optical bandgap and emission intensity of the material. Maximum emission intensity is observed at 1075 °C annealing and a doping level of 0.3 %, while the highest stress luminescence intensity occurs at 0.7 % Pr^{3+} doping.
2. Reusability: although the luminescence intensity of $\text{NaNbO}_3:\text{Pr}^{3+}$ gradually decreased with repeated mechanical stimulation, UV irradiation effectively restored its luminescence performance. This highlights the material's potential for repeated use in anti-counterfeiting applications.
3. Anti-counterfeiting device performance: the device based on 1075 °C annealed $\text{NaNbO}_3:0.7\% \text{Pr}^{3+}$ successfully records dynamic information, including force and speed variations during writing, reflecting the unique writing habits of individual users. This significantly improves the anti-counterfeiting capabilities of electronic signatures.
4. Challenges and future directions: despite its promising performance, the material experiences reduced luminescence intensity under repeated mechanical stimuli, which, although recoverable via UV irradiation, imposes limitations on its application range. Future efforts should focus on developing stress-luminescent materials that maintain stable performance under prolonged use without requiring external restoration methods.

In conclusion, the $\text{NaNbO}_3:\text{Pr}^{3+}$ stress luminescent material presents a significant advancement in personalized electronic signature anti-counterfeiting. Its ability to accurately capture and reflect dynamic signature traits offers a robust solution for enhancing the security and authenticity of electronic signatures.

Acknowledgments

First of all, I would like to thank all the seniors and colleagues in the academic community, whose research results and experience sharing have provided valuable reference and inspiration for the team. It is because of their pioneering research that the team was able to explore and achieve some breakthrough results on this basis. Secondly, I would like to thank all the people and institutions involved in this study, this paper is the result of a team effort, and

their contributions have a crucial impact on the findings of this paper. Finally, I express my sincere gratitude to the reviewers for their invaluable feedback and suggestions, which have greatly contributed to the improvement of my paper.

REFERENCES

1. Zhang, B., Dong, X., Xiong, Y., Zhou, Q., Lu, S., Liao, Y., Yang, Y., Wang, H. A Heat-set Lanthanide Metallogel Capable of Emitting Stable Luminescence under Thermal, Mechanical and Water Stimuli *Dalton Transactions* 49 (9) 2020: pp. 2827–2832. <https://doi.org/10.1039/C9DT04713A>
2. Liu, X., Tan, G., Zhou, Z., Mei, B. Fabrication, Microstructure, Mechanical and Luminescence Properties of Transparent Yb^{3+} -doped $\text{Sr}_5(\text{PO}_4)_3\text{F}$ Nanostructured Ceramics *Journal of the European Ceramic Society* 42 (14) 2022: pp. 6642–6653. <https://doi.org/10.1016/j.jeurceramsoc.2022.07.041>
3. Li, N., Yu, S., Zhao, L., Zhang, P., Wang, Z., Wei, Z., Chen, W., Xu, X. Recoverable Dual-Modal Responsive Sensing Materials Based on Mechanoluminescence and Thermally Stimulated Luminescence toward Noncontact Tactile Sensors *Inorganic Chemistry* 62 (5) 2023: pp. 2024–2032. <https://doi.org/10.1021/acs.inorgchem.2c03540>
4. Xiong, Y., Gong, J., Liu, J., Wang, D., Wu, H., Zhao, Z., Fang, M., Li, Z., Wang, D., Tang, B.Z. Achieving Diversified Emissive Behaviors of AIE, TADF, RTP, Dual-RTP and Mechanoluminescence from Simple Organic Molecules by Positional Isomerism *Journal of Materials Chemistry C* 10 (27) 2022: pp. 10009–10016. <https://doi.org/10.1039/D2TC01857H>
5. Yawalkar, M.M., Nayar, R., Nayar, V., Dhoble, S.J. Synthesis and Mechanoluminescence Study of $\text{Li}_6\text{Y}(\text{BO}_3)_3:\text{Dy}^{3+}/\text{Eu}^{3+}$ Phosphor *Luminescence* 36 (8) 2021: pp. 1851–1861. <https://doi.org/10.1002/bio.3924>
6. Wang, C., Shi, H.Z., Li, W.H., Hu, Q.M., Liu, L., Ren, J., Zhang, J. Interface-Mediated Mechanoluminescence Enhancement from Heterojunction Phosphors: Experiment and Theory *ACS Applied Materials & Interfaces* 15 (25) 2023: pp. 30891–30901. <https://doi.org/10.1021/acsami.3c01282>
7. Chen, F., Jiang, T., Zhai, B., Liu, Y., Yang, X., Wang, X., Ren, F., Tu, D., Ding, T. Mechanoluminescence from an Ion-Irradiated Single Crystal of Lithium Niobium Oxide *The Journal of Physical Chemistry Letters* 13 (24) 2022: pp. 5394–5398. <https://doi.org/10.1021/acs.jpcllett.2c01182>
8. Song, H., Timilsina, S., Jung, J., Kim, T.S., Ryu, S. Improving the Sensitivity of the Mechanoluminescence Composite through Functionalization for Structural Health Monitoring *ACS Applied Materials & Interfaces* 14 (26) 2022: pp. 30205–30215. <https://doi.org/10.1021/acsami.2c07286>
9. Jiang, Y., Shi, Y., Hu, D., Peng, Q., Huang, G., Li, B.S. Insight into Isomeric Effect on the Photoluminescence and Mechanoluminescence of Cyanostilbene Derivatives *The Journal of Physical Chemistry Letters* 13 (33) 2022: pp. 7681–7688. <https://doi.org/10.1021/acs.jpcllett.2c01866>
10. Jayabharathi, J., Thanikachalam, V., Karunakaran, U., Anudeebhana, J., Thilagavathy, S. Mechanoluminescence and Aggregation-Induced Emission in Bipolar

Phenanthroimidazoles: Role of Positional Isomerization-Induced Switching Effect *Industrial & Engineering Chemistry Research* 61 (19) 2022: pp. 6537–6550. <https://doi.org/10.1021/acs.iecr.2c00892>

11. **Yang, Y.L., Li, T., Guo, F., Yuan, J.Y., Zhang, C.H., Zhou, Y., Li, Q.L., Wan, D.Y., Zhao, J.T., Zhang, Z.J.** Multiple Color Emission of Mechanoluminescence and Photoluminescence from SrZnSO: Bi³⁺ for Multimode Anticounterfeiting *Inorganic Chemistry* 61 (10) 2022: pp. 4302–4311. <https://doi.org/10.1021/acs.inorgchem.1c03167>
12. **Tu, L., Xie, Y., Li, Z.** Advances in Pure Organic Mechanoluminescence Materials *The Journal of Physical Chemistry Letters* 13 (24) 2022: pp. 5605–5617. <https://doi.org/10.1021/acs.jpclett.2c01283>
13. **Yuan, J., Yang, Y., Yang, X., Fan, Y., Li, T., Huang, M., Zhang, F., Li, Q., Zhao, J., Zhang, Z.** Regulating the Trap Distribution to Achieve High-contrast Mechanoluminescence with an Extended Saturation Threshold through Co-doping Nd³⁺ into CaZnOS:Bi³⁺,Li⁺ *Journal of Materials Chemistry C* 9 (24) 2021: pp. 7689–7696. <https://doi.org/10.1039/D1TC01815A>
14. **Sicilia, V., Arnal, L., Escudero, D., Fuertes, S., Martin, A.** Chameleonic Photo- and Mechanoluminescence in Pyrazolate-Bridged NHC Cyclometalated Platinum Complexes *Inorganic Chemistry* 60 (16) 2021: pp. 12274–12284. <https://doi.org/10.1021/acs.inorgchem.1c01470>
15. **Ogawa, S., Katsuragi, H., Ikeda, T., Oshima, K., Satokawa, S., Yamazaki, Y., Tsubomura, T.** Dual Mechanoluminescence System Comprising a Solid-state Di-copper(i) Complex Containing N-heterocyclic Carbene Ligands *Dalton Transactions* 50 (25) 2021: pp. 8845–8850. <https://doi.org/10.1039/D1DT00501D>
16. **Kerekes, T.W., You, H., Hemmatian, T., Kim, J., Yun, G.J.** Enhancement of Mechanoluminescence Sensitivity of SrAl₂O₄: Eu²⁺, Dy³⁺/Epoxy Composites by Ultrasonic Curing Treatment Method *Composite Interfaces* 28 (1) 2021: pp. 77–99. <https://doi.org/10.1080/09276440.2020.1740522>
17. **Xu, Z., Li, P., Sun, H., Zhang, Q.** Multicolor Real-time and Differentiation Displays in NaNbO₃-based Photochromics for Advanced Anti-counterfeiting Applications *Ceramics International* 50 (16) 2024: pp. 27661–27670. <https://doi.org/10.1016/j.ceramint.2024.05.164>
18. **Elaiyaraja, P., Karunagaran, N.** The Efficacy of Bi_{0.46}Y_{0.04}K_{0.5}ZrO₃ Doped Three-step Sintering to Accomplish High Piezoelectric and Ferroelectric Properties in New Lead-free NaNbO₃-based Materials *Ceramics International* 50 (3, Part A) 2024: pp. 4810–4822. <https://doi.org/10.1016/j.ceramint.2023.11.224>
19. **Luo, W., Wu, M., Han, Y., Zhou, X., Liu, L., He, Q., Ren, P., Yang, H., Yang, H., Wang, Q., Chen, Z., Liang, X., Chen, Z.** Enhanced Optical Transmittance and Energy-storage Performance in NaNbO₃-modified Bi_{0.5}Na_{0.5}TiO₃ Ceramics *Journal of the American Ceramic Society* 106 (8) 2023: pp. 4723–4731. <https://doi.org/10.1111/jace.19106>



© Wang 2026 Open Access This article is distributed under the terms of the Creative Commons Attribution 4.0 International License (<http://creativecommons.org/licenses/by/4.0/>), which permits unrestricted use, distribution, and reproduction in any medium, provided you give appropriate credit to the original author(s) and the source, provide a link to the Creative Commons license, and indicate if changes were made.